



Porous TiB₂-TiC/TiO₂ heterostructures: Synthesis and enhanced photocatalytic properties from nanosheets to sweetened rolls

Xueqi Guo, Guosong Zhang, Hongzhi Cui*, Na Wei, Xiaojie Song, Jian Li, Jian Tian*

School of Materials Science and Engineering, Shandong University of Science and Technology, Qingdao 266590, China

ARTICLE INFO

Article history:

Received 10 March 2017

Received in revised form 16 May 2017

Accepted 27 May 2017

Available online 29 May 2017

Keywords:

Photocatalytic

Porous TiB₂-TiC

TiO₂ heterostructure

Sweetened roll

ABSTRACT

Exposing high surface areas with porous materials and assembling heterostructures with chemical element doping represent a useful approach to producing high-performance photocatalysts. Porous TiB₂-TiC/TiO₂ heterostructure, a new three-dimensional (3D) porous material with carbon and boron elements, was prepared in this study via alkali-assisted hydrothermal method followed by the in situ growth of porous TiB₂-TiC material. The samples as-formed contain a wide variety of morphologies from nanosheet to sweetened roll, and exhibit dramatically enhanced photocatalytic activity for the degradation of methyl orange and rhodamine B compared to pure porous TiB₂-TiC materials. The mechanisms for heterostructure formation and photocatalytic effect are analyzed to find that the heterostructures enhanced the separation of the photoinduced carriers, and that the morphological features of TiB₂-TiC/TiO₂ heterostructures exert a significant influence on the photocatalytic degradation of organic pollutants.

© 2017 Elsevier B.V. All rights reserved.

1. Introduction

Titanium dioxide (TiO₂) has garnered a great deal of research attention in regards to photochromism, lithium-ion batteries, dye-sensitized solar cells, gas sensors, and photocatalytic degradation [1–4], due to its high chemical stability, abundance, low price, non-toxicity, and extraordinarily high active surface and photocatalytic efficiency [5–8]. Photocatalytic degradation technology is often utilized to remove toxic dyes from wastewater; it is simple, efficient, and economical compared to other treatment processes. Many researchers have explored the synthesis of micro and nanosized photocatalysts with different morphologies [9–12].

The photocatalytic removal of organic pollutants involves illuminating TiO₂ with UV-light to produce electron-hole pairs. After separation, the holes react with water or adsorbed OH[−] and the electrons react with dissolved oxygen to produce hydroxyl and superoxide radicals, respectively [13,14]. The photocatalytic properties of TiO₂ are dependent on their physicochemical properties, not only the crystal phases, particle sizes, and mesoporous structures, but also the exposed active facets and specific surface area, which can significantly affect the material's unique physical and chemical characteristics. TiO₂ exhibits better photocatalytic perfor-

mance when it contains more active facets [15]. TiO₂ microspheres composed of anatase TiO₂ nanosheets with dominant {001} facets can be prepared through a simple thermal treatment resulting in excellent photocatalytic activity for the degradation of organic contaminants and H₂ evolution [16–18].

Composites with large surface area and high porosity are effective precursors for synthesizing porous TiO₂ heterostructures in order to increase active facets and enhance photocatalytic performance. Owing to their high melting point, hardness, high corrosion resistance, low density, good thermal shock resistance, and high temperature stability, TiB₂-TiC composite materials are promising candidates for filter materials, cutting tools, wearproof parts, armored vehicles, and steel matrix reinforcements [19–22]. The favorable properties of porous TiB₂-TiC composites, especially their high porosity and light weight, make them also attractive for use in filtration and adsorption [23,24].

In this paper, TiB₂-TiC composites as raw materials for metal titanium (Ti) were used to fabricate three-dimensional (3D) porous TiB₂-TiC/TiO₂ heterostructures with various morphological features through a facile hydrothermal oxidation route without any additional Ti source. These highly porous TiB₂-TiC composites provided a reaction zone as a support to significantly increase the surface area and enhance the photocatalytic efficiency of TiO₂ via boron and carbon doping. This inherently metastable and nanostructured composite can be converted into a stable, fine-grained microstructure upon re-crystallization during the reaction process. Electrons and holes were likely photogenerated on the surfaces of

* Corresponding authors.

E-mail addresses: cuihongzhi1965@163.com (H. Cui), jiantian@sdust.edu.cn (J. Tian).

TiO₂ in this process. The pores of the TiB₂-TiC/TiO₂ heterostructures provided active reaction sites for photocatalysis and acted as a reservoir of the charge carriers to prolong their lifetime. Interfacial bonding was guaranteed under hydrothermal conditions with the Ti element in porous TiB₂-TiC material, which may minimize the interfacial defects. The reaction rate of methyl orange (MO) and rhodamine B (RhB) dye decomposition was improved through this design. The growth and evolution mechanisms of the TiO₂ microstructures were also analyzed, as discussed below.

2. Experimental procedure

2.1. Materials

Both Ti and B₄C powders with 99% purity were provided by China National Chemicals Corporation Ltd. TiO₂ (P25, 80 wt% anatase, 20 wt% rutile), Sodium hydroxide (NaOH) and hydrochloric acid (HCl) were purchased from Sinopharm. All chemicals used were of analytical reagent grade.

2.2. Preparation of TiB₂-TiC porous composites

Ti and B₄C powders with molar ratio of 3:1 were mixed in a 3D mixing machine, then pressed into pellets with 20 mm diameter and 10 mm height. The compacts were sintered under vacuum at 1350 °C for 2 h; porous TiB₂-TiC composites were also prepared under the same conditions by laser heating for the sake of comparison.

2.3. Preparation of TiB₂-TiC/TiO₂ heterostructure

A patch of porous TiB₂-TiC composites was placed into a 25 mL Teflon-lined stainless steel autoclave filled with 20 mL 1 M NaOH aqueous solution. The sealed autoclave was placed in an electric oven at 220 °C for 2, 6, 12, or 24 h, respectively. After the initial hydrothermal reaction, the pores of TiB₂-TiC composites covered with Na₂Ti₃O₇ nanobelts, nanosheets, or sweetened rolls were immersed in 1 M HCl solution for 1 h to replace Na⁺ with H⁺, resulting in H₂Ti₃O₇ on the pore walls. The samples were rinsed with water and dried in ambient conditions. Finally, the TiO₂ nanobelts, nanosheets, or sweetened rolls were obtained after heat treatment of the H₂Ti₃O₇ in a muffle furnace at 500 °C for 3 h at a heating rate of 2 °C·min⁻¹.

2.4. Characterization

The phase constituents of the synthesized products were analyzed by X-ray diffraction (XRD, D/Max 2500PC Rigaku, Japan) with Cu K_α radiation source. The pore structure and surface characteristics of the products were observed with a high-resolution scanning electron microscope (FESEM, FEI Nova Nanosem 450, USA) equipped with energy dispersive spectroscopy (EDS). High transmission electron microscopy (HRTEM) was carried out with a JEOL JEM 2100F field emission transmission electron microscope. Raman measurements were performed using a Laser Confocal Micro-Raman Spectroscopy equipped with a liquid nitrogen cooled charge-coupled detector. The excitation wavelength is 532 nm from a diode-pumped solid-state laser (LabRAM HR800, FRA). The specific surface area was calculated using the Brunauer-Emmett-Teller (BET) method as-examined on a Micromeritics ASAP2020 nitrogen adsorption-desorption apparatus. The porosity of those products was measured based on the Archimedes principle. The ESR signals were obtained on a Bruker model ER200-SRC spectrometer. The chemical states of the composite were tested using X-ray photoelectron spectrometry measurements (XPS, Thermo ESCALAB 250XI, USA). The UV-vis diffuse reflectance spectra (DRS) of the

samples were tested on a UV-vis spectrophotometer (Hitachi UV-3101) with an integrating sphere attachment within 200–800 nm range and with BaSO₄ as the reflectance standard. Fluorescence lifetimes were measured using the time-correlated single photon counting (TCSPC) technique on a Microtime-200 system (Picoquant) with excitation by a 378 nm laser.

2.5. Photocatalytic activity test

The photocatalytic activity of the TiB₂-TiC/TiO₂ heterostructures was examined in terms of the photodegradation of MO and RhB. In a photodegradation experiment, 50 mg samples were added to 10 mL of aqueous MO (20 mg/L) and RhB (20 mg/L) solutions in an XPA-photochemical reactor (Xujiang Electromechanical Plant, Nanjing, China) with a 300 W mercury lamp as the UV light source. The mixture was first stirred for 30 min in dark conditions, then the solutions were collected after a series of irradiation intervals and the concentration spectrum of the mixture was analyzed with UV-vis spectroscopic measurements (Hitachi UV-3101) after centrifuging.

3. Results and discussions

3.1. Structural characteristics

Fig. 1a shows the XRD patterns of porous TiB₂-TiC composites, where pure TiB₂ and TiC phases exist in the samples produced via laser heating method while TiB and Ti₃B₄ in addition to TiB₂ and TiC phases are observable in the samples produced via sintering reaction under vacuum at 1350 °C. This is because the sintering process did not allow to TiB₂-TiC react completely. The decomposition begin from the surface of B₄C particles per the equation $B_4C \rightarrow 4[B] + [C]$. Based on the decomposition rate, boron-poor phases TiB and Ti₃B₄ form first followed by a small amount of TiB₂. The laser heating method caused the reaction to occur intensely and rapidly at a higher temperature, so the B₄C decompose completely. Thus, boron and carbon atoms combining well with the melt titanium formed the TiB₂-TiC.

Fig. 1b shows the samples prepared via alkali-hydrothermal growth. In addition to TiB₂ and TiC peaks, there are two peaks at 28.3° and 49.2° and five peaks at 24.0°, 30.4°, 31.5°, 37.6°, and 48.5° which are indexed to Na₂Ti₃O₇ (No. 31-1329) and NaB₃O₅ (No. 21-1106), respectively. After H⁺ exchange and calcination at 500 °C for 3 h, the intermediate phases (Na₂Ti₃O₇ and NaB₃O₅) are completely converted to a mixed crystal structure containing anatase and rutile TiO₂ (Fig. 1c), but there is still some unreacted TiB₂ and TiC during the laser heating process. Fig. 1d shows the Raman spectra of TiB₂-TiC/TiO₂ and TiB₂-TiC/Na₂Ti₃O₇ heterostructures prepared via laser heating after hydrothermal reaction at 220 °C for 24 h before or after 500 °C calcination. In the Raman spectra of TiB₂-TiC/TiO₂ heterostructure, the characteristic Raman modes at 144, 398, 514 and 639 cm⁻¹, are attributed to anatase TiO₂ phase [25]; while the characteristic Raman modes at 196, 234 and 444 cm⁻¹, are attributed to rutile TiO₂ phase [26,27]. For TiB₂-TiC/Na₂Ti₃O₇ heterostructure, the obvious peaks appeared are Na₂Ti₃O₇ [28]. Thus, we can differentiate Na₂Ti₃O₇ from TiO₂ successfully.

3.2. Morphology and growth mechanism

The SEM images of the sample pore structures are shown in Fig. 2. Compared to the TiB₂-TiC precursor (Fig. S1), the hydrothermal reaction did not influence the morphology of the porous structures. The average pore size of the samples prepared by the two methods is approximately 10 μm and 40 μm and their porosities are approximately 60% and 72%, respectively, according to the

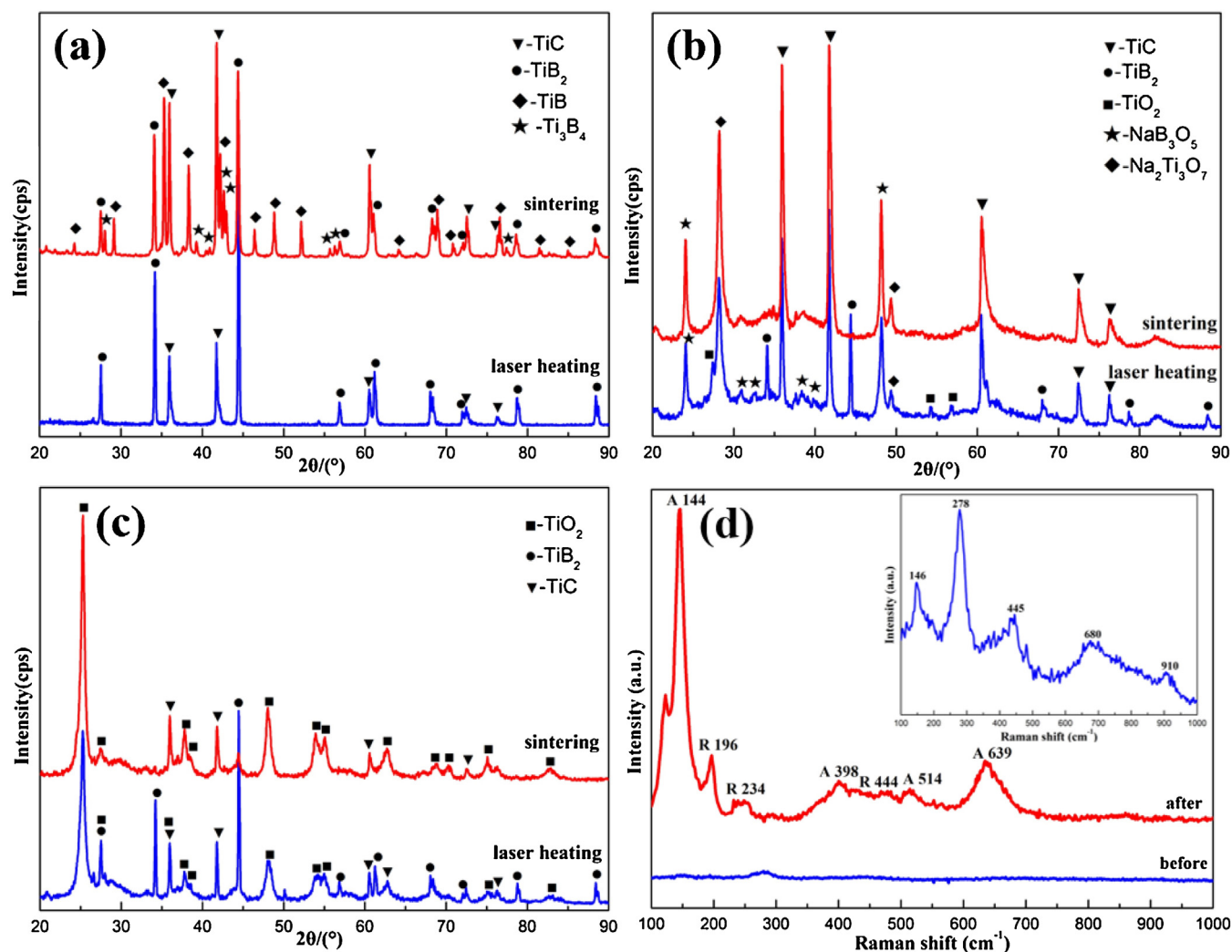


Fig. 1. XRD patterns of (a) TiB₂-TiC, (b) TiB₂-TiC after hydrothermal method at 220 °C for 24 h, (c) TiB₂-TiC/TiO₂ heterostructures after 500 °C calcination, (d) Raman spectra of TiB₂-TiC/TiO₂ (after) and TiB₂-TiC/Na₂Ti₃O₇ (before) heterostructures prepared via laser heating after hydrothermal reaction at 220 °C for 24 h before or after 500 °C calcination. The inset is the alone image of the heterostructure before 500 °C calcination.

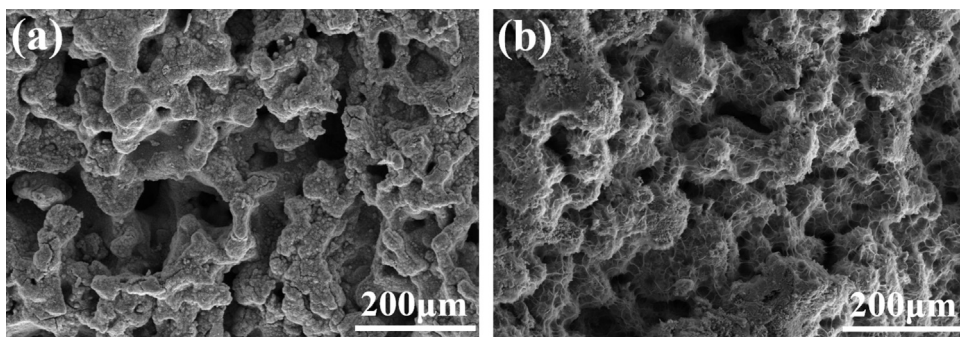


Fig. 2. SEM images of porous TiB₂-TiC precursor after hydrothermal reaction at 220 °C for 24 h, (a) sintering reaction and (b) laser heating.

Archimedes principle. A layer of highly dispersed TiB₂-TiC/TiO₂ heterostructures are assembled on the surface of the TiB₂-TiC porous structure (Fig. 2 and Fig. S2) consisting of TiO₂ nanowires (Fig. 3a and b), nanobelts (Figs. 3c and d), nanorods (Fig. 3e), and nanosheets with thickness of 60–70 nm (Fig. 3f). These heterostructures are stacked together with a 3D porous network. After heat treatment of the heterostructures at 500 °C for 3 h, the morphology and size remained unchanged despite the crystal structure transforming

from body-centered orthorhombic for Na₂Ti₃O₇ (Fig. S3) to body-centered tetragonal for anatase and rutile TiO₂.

We confirm the formation of TiB₂-TiC/TiO₂ microparticles per the removal of the TiB₂-TiC porous structure Ti source as the reaction and the morphology of TiO₂ thickened. The TiB₂-TiC/TiO₂ heterostructures grow and develop as the reaction time progressed from 2 h to 24 h. We observe three significant dimensional morphologies during the hydrothermal reaction leading to different formation mechanisms at different stages of the two methods.

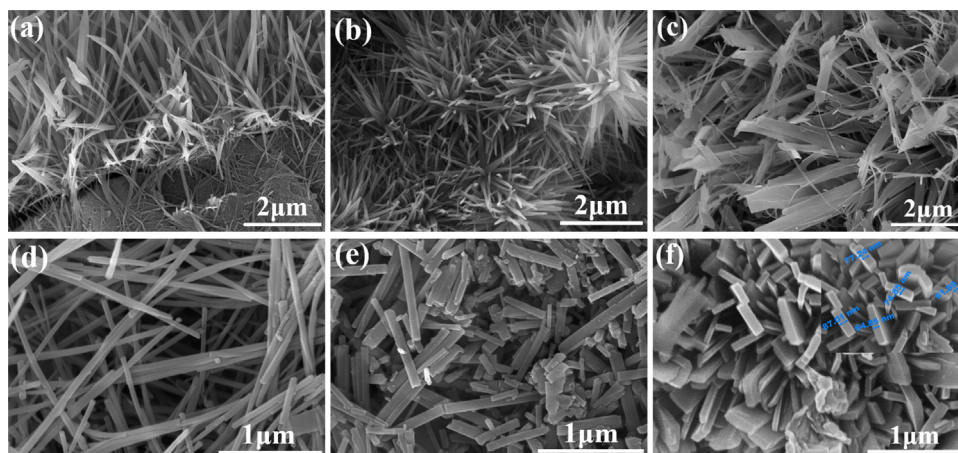


Fig. 3. SEM images of typical $\text{TiB}_2\text{-TiC/TiO}_2$ heterostructures: (a, b) TiO_2 nanowires prepared via laser heating after hydrothermal reaction at 220°C for 2 h; (c, d) TiO_2 nanobelts prepared via sintering after hydrothermal reaction at 220°C for 6 h; (e) TiO_2 nanorods prepared via laser heating after hydrothermal reaction at 220°C for 24 h; (f) TiO_2 nanosheets prepared via sintering after hydrothermal reaction at 220°C for 24 h.

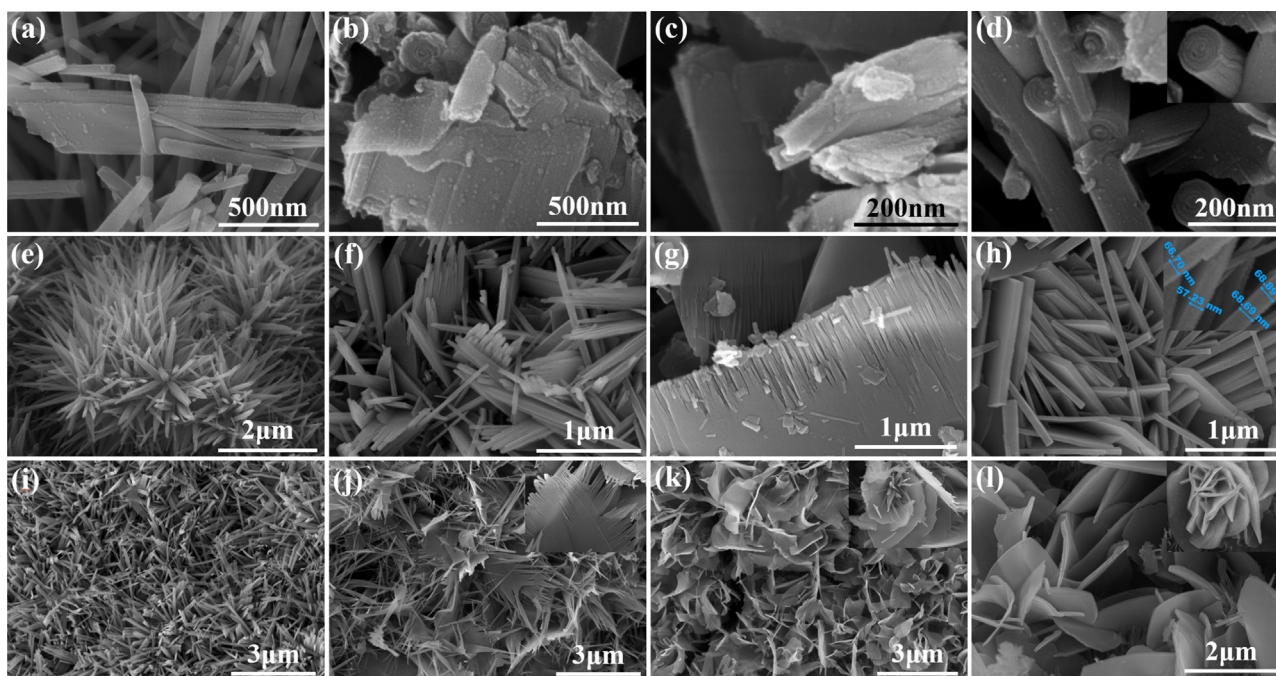


Fig. 4. SEM images of the $\text{TiB}_2\text{-TiC/TiO}_2$ heterostructure formation process: $\text{TiB}_2\text{-TiC/TiO}_2$ sweetened roll heterostructure prepared via laser heating after hydrothermal reaction at 220°C for (a) 2 h, (b) 6 h, (c) 12 h, and (d) 24 h; $\text{TiB}_2\text{-TiC/TiO}_2$ nanosheet heterostructure prepared via laser heating after hydrothermal reaction at 220°C for (e) 2 h, (f) 6 h, (g) 12 h, and (h) 24 h; $\text{TiB}_2\text{-TiC/TiO}_2$ nanosheet heterostructure prepared via sintering after hydrothermal reaction at 220°C for (i) 2 h, (j) 6 h, (k) 12 h, and (l) 24 h.

After 2 h of hydrothermal treatment, thin flat nanobelts (Fig. 4a) and a cloud of slender “needle-like” nanowires (Fig. 4e and i) begin to form on the $\text{TiB}_2\text{-TiC}$ substrate. The nanobelts grow significantly larger, especially in width (Fig. 4b and f). When the reaction time increase to 6 h, the nanowires intersect each other and agglomerate into applanate nanosheets (Fig. 4g). When the hydrothermal reaction time increase to 12 or 24 h, the sample begin to scroll or wrap single-layer nanosheet into a sweetened roll (Fig. 4c). The sweetened rolls are shown in detail in the inset of Fig. 4d. Fig. 4g and h show another SEM image obtained from the thickened, multi-layer TiO_2 nanosheets with average thickness of 60–70 nm, as mentioned above.

During the growth of $\text{TiB}_2\text{-TiC/TiO}_2$ heterostructures via sintering reaction, the single nanosheets curved and assembled into flower-like nanosheets (Fig. 4k and l). There are no significant changes observed when the reaction time increased, which is

attributed to the dramatically decreased NaOH concentration in the thin liquid layer. The SEM images of the samples obtained at longer treatment times indicate a distinctive nanosheet roll-up process. These results suggest that the interaction between nanosheets plays a key role in the surface tension leading to the curvature of the multilayered nanorod structure.

The formation of nanosheets is further assessed by EDS mapping of Ti, Na, O, C, and B. As shown in Fig. 5, square thin sheets are observed, indicating that the heterostructure can be attributed to porous $\text{TiB}_2\text{-TiC}$ and sodium-containing small sheets comprised of $\text{Na}_2\text{Ti}_3\text{O}_7$ (Fig. S5). The carbide sheet contains a large amount of oxygen due to hydroxyl groups terminating the surfaces.

The TEM results (Fig. 6a) indicate that the $\text{TiB}_2\text{-TiC/TiO}_2$ nanorod heterostructure has a rod structure with a diameter of about 70 nm, which conforms to our SEM results (Fig. 3f). As shown in Fig. 6b, the $\text{TiB}_2\text{-TiC/TiO}_2$ nanosheet heterostructure has a sheet-like struc-

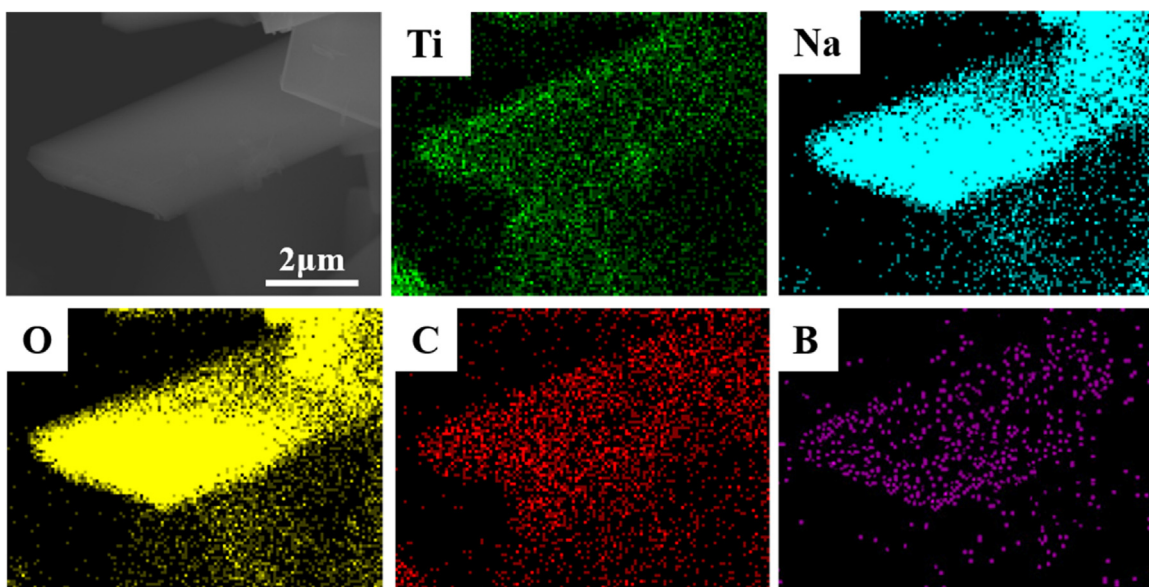


Fig. 5. EDS mapping analysis of $\text{TiB}_2\text{-TiC/TiO}_2$ nanosheet prepared via laser heating after hydrothermal reaction at 220°C for 24 h.

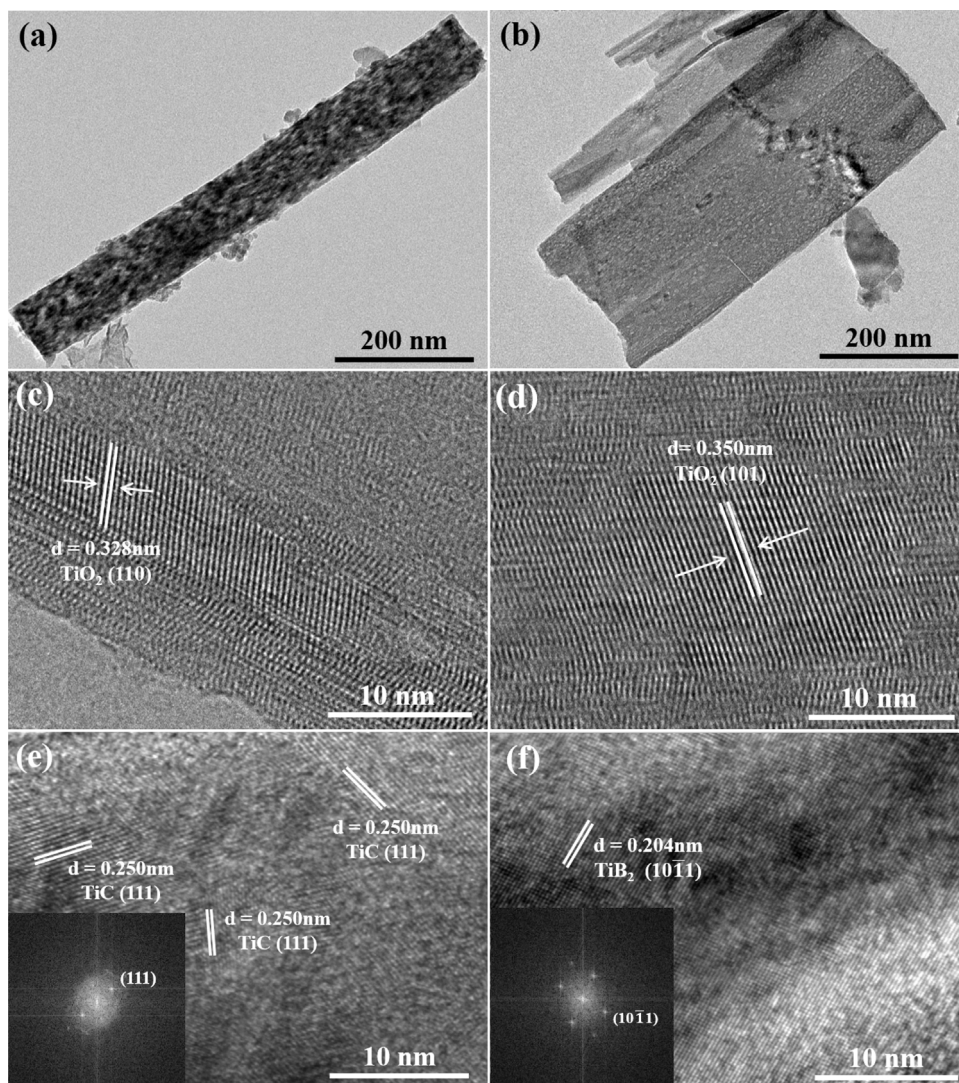
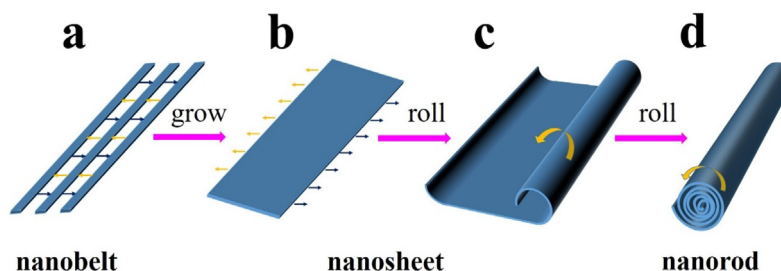


Fig. 6. TEM and HRTEM images of (a, c) $\text{TiB}_2\text{-TiC/TiO}_2$ nanorod heterostructure and (b, d) $\text{TiB}_2\text{-TiC/TiO}_2$ nanosheet heterostructure. HRTEM images of (e) TiC and (f) TiB_2 in the $\text{TiB}_2\text{-TiC/TiO}_2$ heterostructures.



Scheme 1. Schematic illustration of TiO₂ sweetened roll formation.

ture, which is also in accordance with the SEM results (Fig. 4h). The high-resolution TEM images of TiO₂ heterostructures shown in Fig. 6c and d reveal interplanar spacing of 0.350 and 0.328 nm corresponding to the (101) crystal planes of anatase TiO₂ and the (110) crystal planes of rutile TiO₂. In addition, Fig. 6e and f show that the interplanar spacing of TiC and TiB₂ are 0.250 and 0.204 nm corresponding to the (111) and (10 $\bar{1}$ 1) crystal planes respectively.

Scheme 1 shows the formation process of TiB₂-TiC/TiO₂ sweetened roll heterostructures. The TiB₂-TiC porous precursor first reacts with NaOH, forming a highly disordered phase which recrystallizes into some narrow thin plates as a nanobelt (Scheme 1a). Next, the mass nanobelts grow parallel on both sides until overlapping to form an applanate nanosheet (Scheme 1b). The nanosheet then begins to curve and roll itself up. The wrapping of a single nanosheet can also form without a multilayered stack (Scheme 1c). This process ultimately results in the open-ended sweetened roll nanostructures we observed. The SEM images (Fig. 4d) show where the outer shell in these structures is not closed and the inner shell is solid; they also suggest that the nanosheet preferentially grows along the axial direction of the sweetened roll through an oriented crystal growth mechanism (Scheme 1d).

Interestingly, we find that the nanosheets wrapped themselves around one axis to form sweetened rolls: Under hydrothermal conditions, the sweetened rolls are formed via a distinctive nanosheet rollup mechanism that differs markedly from those of conventional nanorod growth processes. Zhang et al. [29] find that single surface layers experience an asymmetrical chemical environment. The driving force for the wrapping may be asymmetry due to preferential doping of the nanosheets with asymmetrical surface forces due to locally high surface energy [30]. In our samples, the imbalance of Na⁺ ion concentration on two different sides of the nanosheet likely creates excess surface energy resulting in bending.

This system can be considered a plane with two springs on each side. When the two sides are placed within a symmetrical chemical environment, both sides experience constant forces, so all tensions are compensated and the plane is straight. When the Na₂Ti₃O₇ nanosheets are in proton-distribution asymmetry, then the sides have different free surface energy. In order to compensate for the imbalance in surface tension, the plane bends into a curve [31]. The excess energy of the system (E_{layer}) can be expressed as the sum of two terms:

$$E_{\text{layer}} = a/R^2 - \beta/R \quad (1)$$

where R is the radius of curvature of the curved nanosheet; a and β are the proportionality constants responsible for the elasticity of the nanosheet and the imbalance in surface tensions, respectively.

The mechanical tension arising during the process of dissolution/crystallization in the nanosheets is also responsible for the bending that we observed. As calculated, the gain in surface energy during wrapping is enough to compensate for mechanical tensions arising due to bending [32]. It is likely that the imbalance in layer width causes the layers to move within the nanosheet and decreases the excess surface energy, causing the nanosheets to

bend. During the simultaneous shift of the layer and bending of the nanosheet, the gain in surface energy is sufficient to compensate for mechanical tension arising in the material during curving and wrapping into sweetened rolls. These findings regarding sweetened roll formation mechanisms may be extended to the fabrication of other metal oxides on desirable substrates for wider applications.

Fig. S5 shows where there are Ti, O, C, and B elements in the TiB₂-TiC/TiO₂ heterostructures and no impurities in the spectra. The XPS spectrum of Ti 2p possesses two strong peaks at the binding energies of 464.6 eV for Ti 2p_{1/2} and 459.0 eV for Ti 2p_{3/2} orbitals of Ti⁴⁺ (Fig. 7a) [33]. In the O 1s spectrum (Fig. 7b), the peak at 530.4 eV can be assigned to lattice oxygen; the shoulder at 532.4 eV corresponds to the defects due to oxides or a mixture of hydroxyl groups on the surface of the catalysts [34], while the peaks at 284.8 eV and 286.5 eV can be assigned to the C 1s orbitals of C–C and C–O, respectively (Fig. 7c) [35–40]. As shown in Fig. 7d, one peak observed at 192.7 eV is assigned to B 1s [41].

3.3. Photocatalytic decomposition of MO and RhB

The photocatalytic activities of the prepared samples were investigated per the decomposition of MO and RhB dye under UV light irradiation. For comparison, TiB₂-TiC porous composites and P25 powder were used as photocatalytic references under the same experimental conditions; the results are shown in Fig. 8a and b, respectively. The TiB₂-TiC/TiO₂ heterostructures exhibit more prominent photocatalytic activity compared to the porous TiB₂-TiC alone. After 3 h of irradiation with UV light, MO and RhB are almost entirely decomposed by the TiB₂-TiC/TiO₂ heterostructures prepared via laser heating method, i.e., this sample shows much higher degradation efficiency than the sintering reaction method and P25. The favorable performance can be ascribed to the high surface area of the porous material, where the heterostructures grow on the substrate as an ordered film without agglomeration compared to the porous TiB₂-TiC. Photocatalytic performance is enhanced by the higher amount of anatase TiO₂ and higher average surface energy of the laser-heated sample [42] as well as the abundance of nanorods, as evidenced by XRD (Fig. 1c) and SEM results (Fig. 4). Fig. 4 shows that a large number of sweetened roll heterostructures are formed after hydrothermal reaction for 24 h, and most of them are nanosheet heterostructures at 12 h, with only a few sweetened roll heterostructures. So, we also compare the sample prepared via laser heating after hydrothermal reaction at 220 °C for 12 h and 24 h for photocatalytic degradation of MO and RhB (Fig. S6). As we can see the TiB₂-TiC/TiO₂ heterostructures prepared via laser heating after hydrothermal reaction at 220 °C for 24 h show better photocatalytic performance. So that the sweetened roll heterostructures show the better photocatalytic performance than the nanosheet heterostructures.

The UV–vis DRS of TiB₂-TiC/TiO₂ heterostructures prepared by two methods are examined to further assess the changes in their photocatalytic activity, as shown in Fig. 8c. The TiB₂-TiC composite shows almost no absorption of the UV region but there is

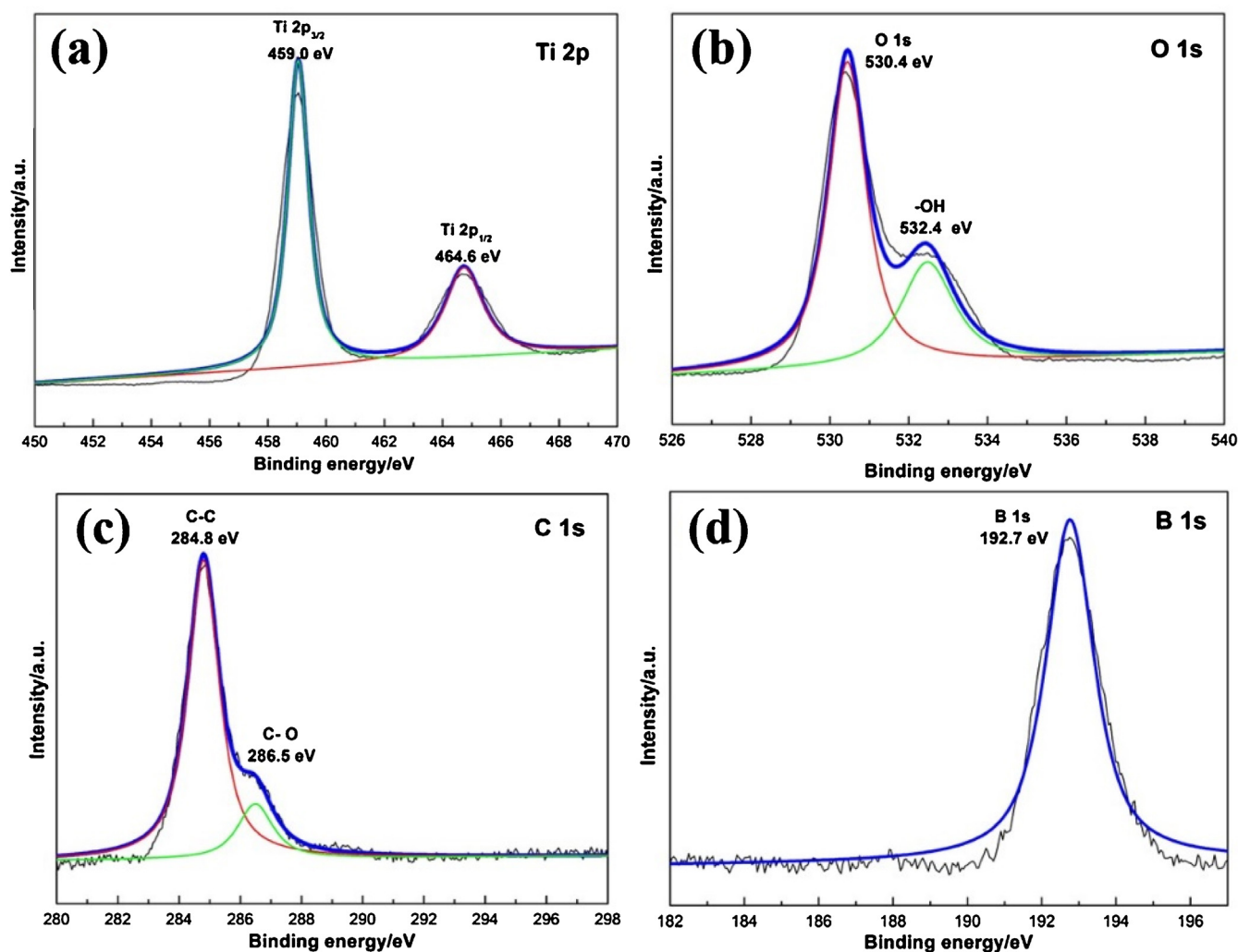


Fig. 7. X-ray photoelectron spectra: (a) Ti 2p, (b) O 1s, (c) C 1s, and (d) B 1s in $\text{TiB}_2\text{-TiC/TiO}_2$ heterostructures prepared via laser heating after hydrothermal reaction at 220°C for 24 h.

enhanced absorption of the $\text{TiB}_2\text{-TiC/TiO}_2$ heterostructures at the same region. This increase in absorption resulted in an improvement to the UV photocatalytic properties of the $\text{TiB}_2\text{-TiC/TiO}_2$ heterostructures.

The time-resolved fluorescence decay spectra of the samples showing the excitation and transfer process are shown in Fig. 8d. There is an overall increase in photogenerated charge carrier lifetimes in the $\text{TiB}_2\text{-TiC/TiO}_2$ heterostructures. The transient signal strength of $\text{TiB}_2\text{-TiC/TiO}_2$ heterostructures produced via laser heating is stronger compared to the other sample. They are $\tau_1 = 1.01$, 1.07 and 1.15 ns respectively. The recombination of electrons with free holes results in a rapid decay. The surface hydroxyl groups capture trapped holes to separate the electrons and holes, causing a slow decay [43].

Fig. 9a and b show the electron spin resonance (ESR) spectra measured as the effect of light irradiation on the $\text{TiB}_2\text{-TiC/TiO}_2$ heterostructures, which are gathered to investigate the reactive oxygen species generated during the photodegradation of MO and RhB. There are no signals when the system was in the dark, while both signals of $\text{DMPO} \cdot \text{O}_2^-$ and $\text{DMPO} \cdot \text{OH}$ are clearly observed once the heterostructures are irradiated under UV light. The $\cdot\text{O}_2^-$ and $\cdot\text{OH}$ signal intensities of the system increased with extended irradiation time, suggesting that $\cdot\text{O}_2^-$ and $\cdot\text{OH}$ are major oxidation active species in the sample. These observations elucidate the

mechanism at work in the photocatalytic process involving the oxidation of both $\cdot\text{OH}$ and $\cdot\text{O}_2^-$ radicals.

The DRS results of the TiB_2 , TiC and TiO_2 are shown in Fig. S7. The estimated E_g (bandgap energy) of TiB_2 , TiC and TiO_2 is 0, 0 and 3.2 eV, respectively. Both TiB_2 and TiC have good conductivity and no band gap [44,45]. Under UV light irradiation, TiO_2 in the $\text{TiB}_2\text{-TiC/TiO}_2$ composite can be excited to generate electrons and holes (Scheme 2). The electrons can transport into the $\text{TiB}_2\text{-TiC}$ part, the holes in the TiO_2 would take part in photocatalysis under UV light irradiation as a result of better photogenerated carriers separation, which can react with O_2 and H_2O to form $\cdot\text{O}_2^-$ and $\cdot\text{OH}$, and directly oxidize the pollutants [46,47]. The enhanced photocatalytic property of the $\text{TiB}_2\text{-TiC/TiO}_2$ heterostructures, especially those prepared by the laser heating method, can be attributed to: 1) The band gap of TiO_2 [48] lending the heterostructure superior UV absorption ability, promotes the separation of photo-generated carriers [49,50] and introduces more active species for photocatalysis. 2) The high specific surface area of $\text{TiB}_2\text{-TiC/TiO}_2$ heterostructures, which offers more active sites for pollutant molecule absorption and facilitates the improvement of photocatalytic properties [51,52]; the BET surface area of the heterostructures produced via laser heating is about $24.9\text{ m}^2\cdot\text{g}^{-1}$, which is larger than that of the sintering reaction sample ($22.1\text{ m}^2\cdot\text{g}^{-1}$). 3) The high-energy facets of $\text{TiB}_2\text{-TiC/TiO}_2$

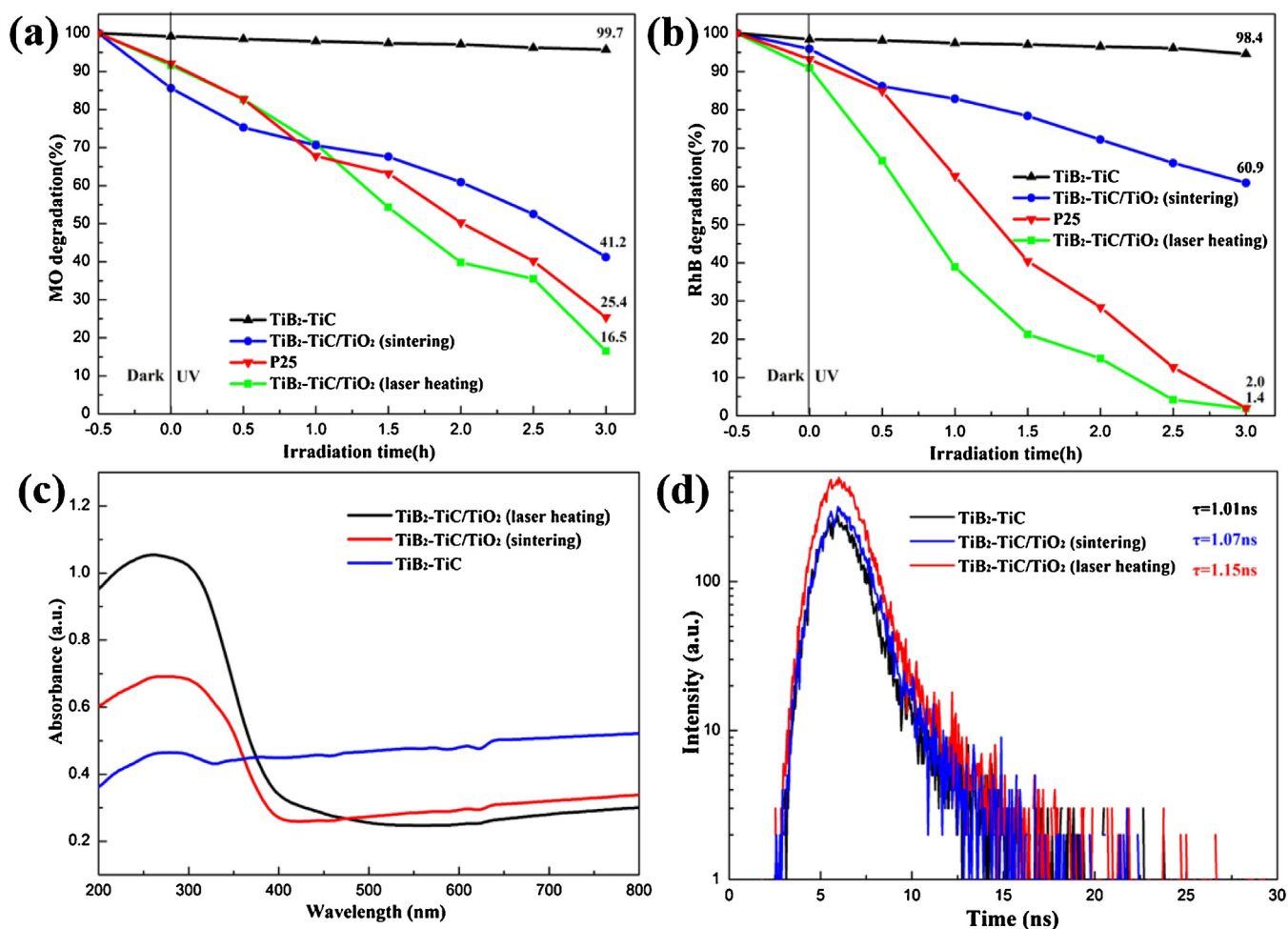


Fig. 8. Photocatalytic decomposition of (a) MO (b) RhB in the presence of samples under UV light; (c) UV-vis diffuse reflectance spectra of porous $\text{TiB}_2\text{-TiC}$ precursor and $\text{TiB}_2\text{-TiC/TiO}_2$ heterostructures; (d) Time-resolved fluorescence decay spectra of $\text{TiB}_2\text{-TiC}$ precursor and $\text{TiB}_2\text{-TiC/TiO}_2$ heterostructures for emission at 475 nm and excitation at 378 nm.

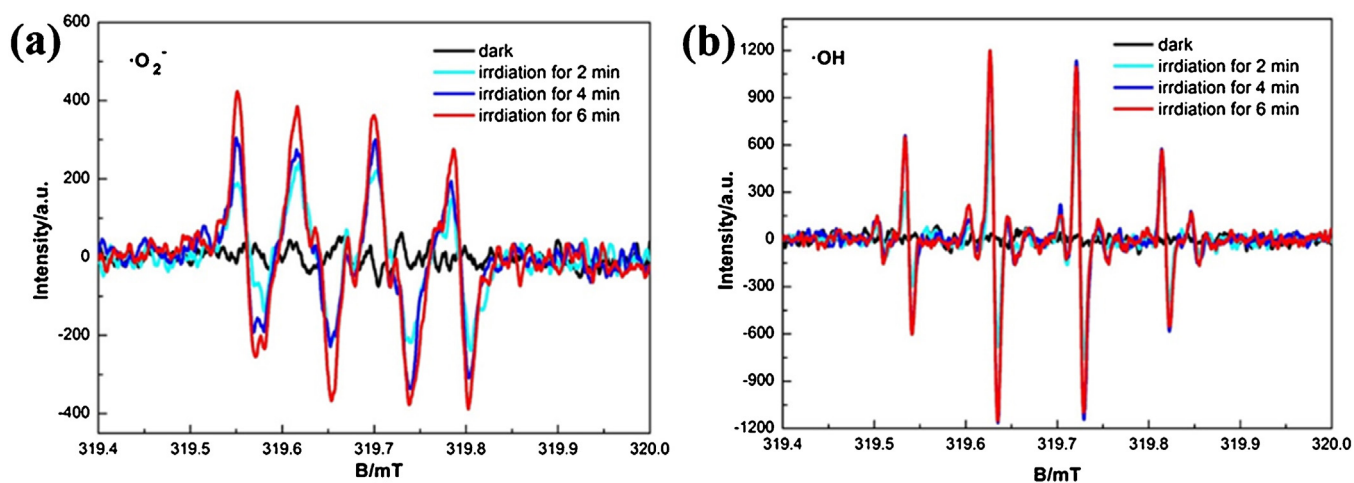
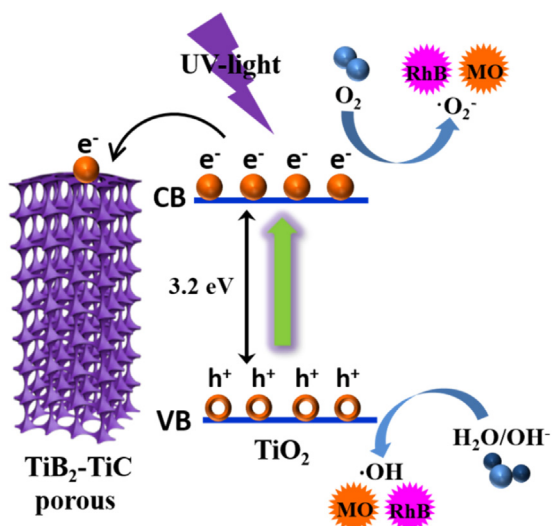


Fig. 9. DMPO spin-trapping ESR spectra of $\text{TiB}_2\text{-TiC/TiO}_2$ heterostructures in methanol dispersion for (a) DMPO- $\cdot\text{O}_2^-$ and (b) DMPO- $\cdot\text{OH}$ under UV light irradiation.

heterostructures prepared by laser heating constitute all the side faces, so exposing them to the reagent in a radial and arc surface distribution (as opposed to a planar structure) is the ideal morphology in terms of photoactivity. The electron transfer also slows

the recombination of photo-induced charge carriers and prolongs the electron lifetime, which may be an important reason of the favorable photoactivity of the $\text{TiB}_2\text{-TiC/TiO}_2$ heterostructures.



Scheme 2. Schematic photocatalytic mechanism for the $\text{TiB}_2\text{-TiC}/\text{TiO}_2$ heterostructures under UV light irradiation.

4. Conclusions

We used two different methods, sintering reaction and laser heating, to prepare the $\text{TiB}_2\text{-TiC}$ precursors and demonstrated a facile, template-free hydrothermal method for preparing porous $\text{TiB}_2\text{-TiC}/\text{TiO}_2$ heterostructures with enhanced UV photocatalytic performance. By simply adjusting the hydrothermal reaction time, shape-controlled nanostructures from nanosheet to sweetened roll can be obtained. Also, the TiO_2 sweetened rolls are formed by a distinctive nanosheet roll-up mechanism under hydrothermal conditions. The as-prepared porous $\text{TiB}_2\text{-TiC}/\text{TiO}_2$ heterostructures show several advantageous structural features: A more porous structure with high surface area and an abundance of reactive nanorod facets, which result in enhanced UV photocatalytic performance for MO and RhB degradation. Combining the advantages of porous $\text{TiB}_2\text{-TiC}/\text{TiO}_2$ heterostructures, the hybrid structure is a promising candidate for practical applications in many fields such as water splitting, organic solar cells, and lithium ion batteries due to its simplicity, cost-effectiveness, and scaled-up preparation process.

Acknowledgments

The authors are thankful for fundings from the National High Technology Research and Development Program of China (863 Program, No. 2015AA034404), Distinguished Taishan Scholars in Climbing Plan (No. tspd20161006), Science and Technology Development Planning of Shandong Province (No. 2014GGX102026), National Natural Science Foundation of China (No. 51502160), Applied Basic Research Foundation of Qingdao City (No. 16-5-1-93-jch), and SDUST Research Fund (No. 2015JQJH101).

Appendix A. Supplementary data

Supplementary data associated with this article can be found, in the online version, at <http://dx.doi.org/10.1016/j.apcatb.2017.05.079>.

References

- [1] Y. Bai, P.Y. Luo, P.Q. Wang, J.Y. Liu, Catal. Commun. 37 (2013) 45–49.
- [2] J.S. Chen, Y.L. Tan, C.M. Li, Y.L. Cheah, D. Luan, S. Madhavi, F.Y.C. Boey, L.A. Archer, X.W. Lou, J. Am. Chem. Soc. 132 (2010) 6124–6130.

- [3] J. Moon, J.A. Park, S.-J. Lee, T. Zyung, I.D. Kim, Sens. Actuators, B 149 (2010) 301–305.
- [4] L. Zhao, X. Chen, X. Wang, Y. Zhang, W. Wei, Y. Sun, M. Antonietti, M.M. Titirici, Adv. Mater. 22 (2010) 3317–3321.
- [5] B. Mazinan, A. Beitollahi, S. Radiman, A.K. Masrom, S.M. Ibrahim, J. Javadpour, F.M. Jamil, J. Alloy. Compd. 519 (2012) 72–76.
- [6] H. Xia, H. Zhuang, D. Xiao, T. Zhang, J. Alloy. Compd. 465 (2008) 328–332.
- [7] Y. Yan, X. Qiu, H. Wang, L. Li, X. Fu, L. Wu, G. Li, J. Alloy. Compd. 460 (2008) 491–495.
- [8] Y. Zhao, C. Li, X. Liu, F. Gu, J. Alloy. Compd. 440 (2007) 281–286.
- [9] A.A. Jalil, S. Triwahyono, S.H. Adam, N.D. Rahim, M.A. Aziz, N.H. Hairom, N.A. Razali, M.A. Abidin, M.K. Mohamadiah, J. Hazard. Mater. 181 (2010) 755–762.
- [10] S. Lan, N. Guo, L. Liu, X. Wu, L. Li, S. Gan, Appl. Surf. Sci. 283 (2013) 1032–1040.
- [11] O. Mohanta, Y.N. Singhababu, S.K. Giri, D. Dadhich, N.N. Das, R.K. Sahu, J. Alloy. Compd. 564 (2013) 78–83.
- [12] J. Tian, Y. Leng, H. Cui, H. Liu, J. Hazard. Mater. 299 (2015) 165–173.
- [13] C.B.D. Marrien, T. Cottineau, D. Robert, P. Drogui, Appl. Catal. B-environ. 194 (2015) 1–6.
- [14] J. Tian, X. Hu, N. Wei, Y. Zhou, X. Xu, H. Cui, H. Liu, Sol. Energ. Mat. Sol. C 151 (2016) 7–13.
- [15] Z. Zheng, B. Huang, X. Qin, X. Zhang, Y. Dai, M. Jiang, P. Wang, M.H. Whangbo, Chem.-A Eur. J. 15 (2009) 12576–12579.
- [16] J. Zhao, X.X. Zou, J. Su, P.P. Wang, L.J. Zhou, G.D. Li, J. Chem. Soc. Dalton 42 (2013) 4365–4368.
- [17] M. Pelaez, N.T. Nolan, S.C. Pillai, M.K. Seery, P. Falaras, A.G. Kontos, P.S.M. Dunlop, J.W.J. Hamilton, J.A. Byrne, K. O'Shea, Appl. Catal. B-environ. 125 (2012) 331–349.
- [18] X. Zhang, G. Zuo, X. Lu, C. Tang, S. Cao, M. Yu, J. Colloid Interf. Sci. 490 (2017) 774–782.
- [19] H. Cui, W. Liu, L. Cao, Q. Song, J. Tian, F. Teng, J. Wang, J. Eur. Ceram. Soc. 35 (2015) 3381–3388.
- [20] Y.H. Liang, H.Y. Wang, Y.F. Yang, Y.L. Du, Q.C. Jiang, J. Int. H. Refract. Met. 26 (2008) 383–388.
- [21] L. Ma, H.Z. Cui, L.L. Cao, F.L. Teng, N. Cui, L. Liu, J. Adv. Mater. 634–638 (2013) 2110–2118.
- [22] H. Cui, Y. Zhang, G. Zhang, W. Liu, X. Song, N. Wei, Ceram. Int. 42 (2016) 8376–8384.
- [23] C. Peng, X. Yang, Y. Li, H. Yu, H. Wang, F. Peng, ACS Appl. Mat. Interfaces. 8 (2016) 6051–6060.
- [24] X. Zhang, X. Zhao, D. Wu, Y. Jing, Z. Zhou, Nanoscale 7 (2015) 16020–16025.
- [25] N. Wei, H. Cui, C. Wang, G. Zhang, Q. Song, W. Sun, X. Song, M. Sun, J. Tian, J. Am. Ceram. Soc. 100 (2017) 1339–1349.
- [26] X. Han, X. Han, L. Sun, P. Wang, M. Jin, X.J. Wang, Mater. Chem. Phys. 171 (2016) 11–15.
- [27] V. Swamy, Phys. Rev. B 77 (2008) 998–1002.
- [28] Á. Kukovec, M. Hodos, E. Horváth, G. Radnóczi, Z. Kónya, I. Kiricsi, J. Phys. Chem B 109 (2005) 17781–17783.
- [29] S. Zhang, L.M. Peng, Q. Chen, G.H. Du, G. Dawson, W.Z. Zhou, Phys. Rev. Lett. 91 (2004) 12475–12493.
- [30] D. Wu, J. Liu, X. Zhao, A. Li, A. Yanfeng Chen, N. Ming, Chem. Mater. 18 (2005) 533–547.
- [31] D.V. Bavykin, J.M. Friedrich, F.C. Walsh, J. Adv. Mater. 18 (2010) 2807–2824.
- [32] D.V. Bavykin, V.N. Parmon, A.A. Lapkin, F.C. Walsh, J. Mater. Chem. 14 (2004) 3370–3377.
- [33] B. Sambandam, A. Surendran, L. Philip, T. Pradeep, ACS Sustain. Chem. Eng. 3 (2015) 1321–1329.
- [34] Y. Zhang, S. Yuan, Y. Zhao, H. Wang, C. He, J. Mater. Chem. 2 (2014) 7897–7903.
- [35] E. Benko, T.L. Barr, S. Hardcastle, E. Hoppe, A. Bernasik, J. Morgiel, Ceram. Int. 27 (2001) 637–643.
- [36] X.H. Gao, Z.M. Guo, Q.F. Geng, P.J. Ma, G. Liu, Sol. Energ. Mat. Sol. C 157 (2016) 543–549.
- [37] A.A.E. Mel, B. Angleraud, E. Gautron, A. Granier, P.Y. Tessier, Thin Solid Films 519 (2011) 3982–3985.
- [38] D.M.D. Narvaez, J.M.G. Carmona, A.R. Muñoz, Rev. Mex. Fis. 59 (2013) 90–94.
- [39] R. Rani, N. Kumar, D.D. Kumar, K. Panda, S.K. Srivastava, S. Dash, A.K. Tyagi, Tribol. Int. 104 (2016) 121–130.
- [40] J.S. Stevens, A.C. Luca, M. Pelendritis, G. Terenghi, S. Downes, S.L.M. Schroeder, Surf. Interface. Anal. 45 (2014) 1238–1246.
- [41] C. Jayanthi, S. Dhanapandian, K.R. Murali, Front. Mater. Sci. 7 (2013) 379–386.
- [42] W. Guo, F. Zhang, C. Lin, Z.L. Wang, J. Adv. Mater. 24 (2012) 4761–4764.
- [43] J. Li, H. Cui, X. Song, N. Wei, J. Tian, Appl. Surf. Sci. 396 (2017) 1539–1545.
- [44] M. Kumar, G.K. Gupta, O.P. Modi, B.K. Prasad, A.K. Khare, M. Sharma, Can. Metall. Quart. 56 (2017) 58–66.
- [45] M.A. Zavareh, A.A.D.M. Sarhan, M.A. Roudan, P.A. Zavareh, IJRSE 27 (2014) 2347–3207.
- [46] X. Hu, Y. Li, J. Tian, H. Yang, H. Cui, J. Ind. Eng. Chem. 45 (2017) 189–196.
- [47] J. Tian, P. Hao, N. Wei, H. Cui, H. Liu, ACS Catal. 5 (2015) 4530–4536.
- [48] S. Shen, Y. Zhang, L. Peng, Y. Du, Q. Wang, Angew. Chem. Int. Edit. 50 (2011) 7115–7118.
- [49] W.L. Ong, M. Gao, G.W. Ho, Nanoscale 5 (2013) 11283–11290.
- [50] L. Zhu, M. Hong, G.W. Ho, Nano Energy 11 (2015) 28–37.
- [51] J. Tian, J. Li, N. Wei, X. Xu, H. Cui, H. Liu, Ceram. Int. 42 (2015) 1611–1617.
- [52] N. Wei, H. Cui, Q. Song, L. Zhang, X. Song, K. Wang, Y. Zhang, J. Li, J. Wen, J. Tian, Appl. Catal. B-environ. 198 (2016) 83–90.